ACS OMEGA

Article

Cite This: ACS Omega 2018, 3, 18943−18949

http://pubs.acs.org/journal/acsodf

Uniform Vapor-Pressure-Based Chemical Vapor Deposition Growth of MoS_2 Using MoO_3 Thin Film as a Precursor for Coevaporation

Sajeevi S. Withanage,[†,‡] Hirokjyoti Kalita,[‡,∥] Hee-Suk Chung,[⊥] Tania Roy,[‡,§,∥] Yeonwoong Jung,[‡,§,∥] and Saiful I. Khondaker*[,†,‡,∥]

[†]Department of Physics, University of Central Florida, 4111 Libra Drive, Physical Sciences Bldg. 430, Orlando, Florida 32816, United States

[‡]NanoScience Technology Center, University of Central Florida, Research Pkwy #400, Orlando, Florida 12424, United States

[§]Department of Materials Science & Engineering, University of Central Florida, 12760 Pegasus Drive, Engineering I, Suite 207, Orlando, Florida 32816, United States

[∥]Department of Electrical & Computer Engineering, University of Central Florida, 4328 Scorpius Street, Orlando, Florida 32816, United States

[⊥]Analytical Research Division, Korea Basic Science Institute, Geonji-road 20, Jeonju 54907, South Korea

Supporting Information

ABSTRACT: Chemical vapor deposition (CVD) is a powerful method employed for high-quality monolayer crystal growth of 2D transition metal dichalcogenides with much effort invested toward improving the growth process. Here, we report a novel method for CVD-based growth of monolayer molybdenum disulfide (MoS_2) by using thermally evaporated thin films of molybdenum trioxide (MoO_3) as the molybdenum (Mo) source for coevaporation. Uniform evaporation rate of MoO_3 thin films provides uniform Mo vapors which promote highly reproducible single-crystal growth of MoS_2 throughout the substrate. These high-quality crystals are as large as 95 μm and are characterized by scanning electron microscopy, Raman spectroscopy, photoluminescence spectroscopy, atomic force microscopy, and transmission electron microscopy. The bottom-gated field-effect transistors fabricated using the as-grown single crystals show n-type transistor behavior with a good on/off ratio of 10^6 under ambient conditions. Our results presented here address the precursor vapor control during the CVD process and is a major step forward toward reproducible growth of MoS_2 for future semiconductor device applications.

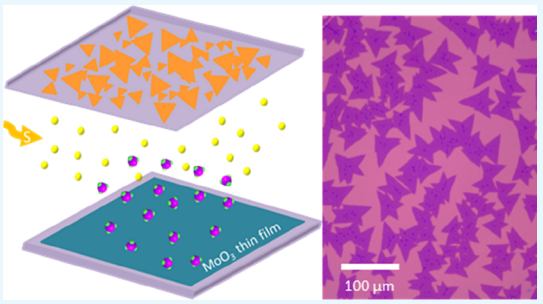

INTRODUCTION

Layered two-dimensional (2D) semiconducting transition metal dichalcogenides (TMDCs) (MX_2: M = Mo, W, X = S, Se, Te) have attracted a great deal of attention because of their exciting properties emerging from quantum confinement effects including intrinsic direct band gap in a single layer, high photoconductivity,[1,2] appreciable charge mobility, and high on/off ratio.[3] In particular, 2D molybdenum disulfide (MoS_2) has been studied extensively over the past few years because of its natural abundance and making expedited progress in its applications in the fields of electronics and optoelectronics with photodetectors,[4] light-emitting devices,[5] solar cells,[6] and biosensors.[7−9] Most of these studies were carried out in exfoliated samples which limit their practical application because of low yield, small lateral size, and uncontrolled layer number. For scalable device fabrication, large-scale synthesis of MoS_2 is highly desirable. Chemical vapor deposition (CVD)-based synthesis methods including thermal vapor sulfurization of Mo/MoO_3 films,[10−12] thermal decomposition of thiosalts,[13] and gas phase reaction of $MoCl_5$ and H_2S gas[14] have been employed for large-scale synthesis; however, obtaining MoS_2 samples with controlled layer number and high electrical and optical quality remain elusive with these methods. The coevaporation of Mo and S precursor-based CVD has received much attention for the past few years because of its ability to produce high-quality MoS_2 single crystals with excellent electrical and optical properties.[15−18] The challenging nature of CVD growth of MoS_2 continues to stimulate intense research effort in this field. If the CVD is going to be used for large-scale production of MoS_2 samples, it is important to understand how small variations of CVD process parameters could lead to different results.[19,20]

In the coevaporation-based CVD technique, the MoO_3 powder and the S powder are commonly used to produce Mo and S vapors which then react to produce MoS_2 crystal, following the two-step chemical reactions.[21]

Received: October 28, 2018
Accepted: December 19, 2018
Published: December 31, 2018

DOI: 10.1021/acsomega.8b02978
ACS Omega 2018, 3, 18943−18949

$$MoO_3 + \frac{x}{2}S \rightarrow MoO_{3-x} + \frac{x}{2}SO_2$$

$$MoO_{3-x} + \frac{7-x}{2}S \rightarrow MoS_2 + \frac{3-x}{2}SO_2$$

Because most of the growth-related reactions occur in the vapor phase, the uniform melting/sublimation of the precursors and maintaining uniform vapor pressure of the gas-phase precursors are highly desirable for clean and reproducible growth of MoS_2. However, such a control of uniform vapor pressure turned out to be very challenging, resulting in a growth of oxide/oxysulfide (MoO_2/$MoOS_2$) species along with MoS_2.[19,22] To our knowledge, the importance of controlling sulfur vapor pressure is discussed in detail in the literature,[23,24] but the discussion of controlling Mo vapor pressure is rare. In particular, having a uniform vapor pressure of Mo in the reaction region when sulfur enters can help to maintain proper Mo/S ratio for the successful and reproducible growth of MoS_2. However, when small amount of MoO_3 powder is used and because of the different particle sizes in the powder, MoO_3 cannot be uniformly distributed in the crucible which might hinder clean and reproducible growth of MoS_2.

Here, we show that by replacing MoO_3 powder with a MoO_3 thin film for Mo precursors, clean and reproducible growth of monolayer MoS_2 can be obtained. MoO_3 thin film of 5−20 nm was thermally evaporated from MoO_3 powder which was then used as the Mo precursor for coevaporation. Uniform evaporation rate of our thin-film precursor facilitates better control of Mo vapor in the vapor phase, resulting in clean triangular crystals of monolayer MoS_2 on Si/SiO_2 substrates with a high crystal quality and uniformity proved by scanning electron microscopy (SEM), Raman spectroscopy, photoluminescence (PL) spectroscopy, atomic force microscopy (AFM), and transmission electron microscopy (TEM). Electric characterization of these pristine crystals with bottom-gated field-effect transistors (FETs) showed an n-type transistor behavior with a good on/off ratio of 10^6 under ambient conditions, verifying the ability of these materials in modern semiconductor electronics.

RESULTS

We synthesized MoS_2 single crystals in a home-built atmospheric pressure CVD system. Figure 1a shows our experimental setup for this study. MoO_3 thin films were deposited on Si/SiO_2 substrate using thermal evaporation and used as the Mo source for coevaporation synthesis of MoS_2 crystals in a single-zone tube furnace. Substrates were placed faced down toward the thin film source. Sulfur was placed upstream at a low-temperature zone. The temperature profiles for MoO_3 and S are shown in Figure 1c. Further information on the growth process can be found in the Materials and Methods section.

Figure 2 shows a representative result for our optimized CVD growth of MoS_2. For this, we used 20 nm thin film of MoO_3 as a precursor for Mo vapor. S was placed at the edge of the furnace, 23.5 cm upstream from the center of the furnace, and the growth temperature was 750 °C. Figure 2a shows an optical image of the whole Si/SiO_2 substrate after MoS_2 growth as well as a bare substrate for comparison. The darker region of the growth substrate is where the crystals are grown. This region of the substrate is directly facing toward the thin-film MoO_3 source. To show the growth on this substrate in

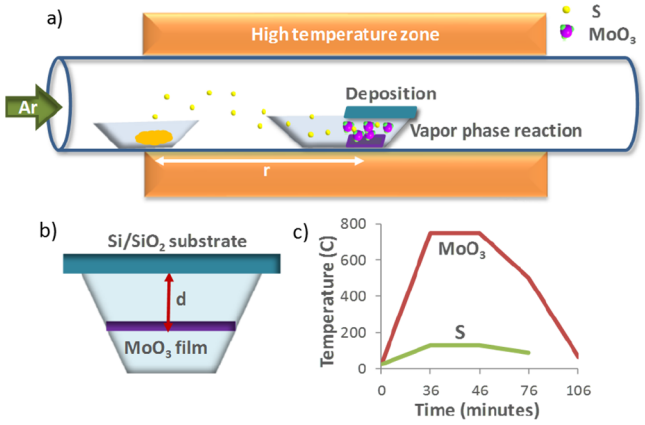

Figure 1. Experimental setup. (a) Schematic representation of the atmospheric pressure CVD setup and the relative S, MoO_3, and substrate positioning. (b) Cross-sectional view of the substrate boat: target substrate was placed face down toward the film at a small distance *d*. (c) Temperature profile of MoO_3 and S at a setpoint value of 750 °C.

detail, we divided this region into nine sections, as shown in Figure 2b, and presented optical micrographs of each of these region (labeled 1−9) in Figure 2d. From here, we see that dense crystal grains of self-seeded MoS_2 are grown throughout the growth substrate without any traces of MoO_2/$MoOS_2$. This is in clear contrast to what we have observed when we used a small amount of (∼1 mg) MoO_3 powder as a Mo precursor, where we saw isolated regions of MoS_2 growth along with rhomboidal MoO_2/$MoOS_2$ on MoS_2 in other regions (Figure S1). Increasing amount of MoO_3 powder only increased the regions of MoO_2/$MoOS_2$. Because the difference between the two scenarios is the uniform sublimation of MoO_3 thin film which causes uniform evaporation of Mo in the growth region, we conclude that uniform evaporation of Mo has an important role in dense singe-crystal growth of MoS_2. We repeated the MoO_3 thin film growth over 50 times, and we always obtained clean MoS_2 growth without any oxysulfides. This was not the case when we used MoO_3 powder, where clean and reproducible MoS_2 crystals were hard to achieve. Another important observation is that all of the single crystals are triangular in shape. Given the conditions of the growth and the rough edges of these triangular crystals (Figure 3b) which are S-zz terminations, we conclude that they are grown at a sulfur-sufficient environment.[24,25] The shape and size variation of MoS_2 crystals has been discussed in the literature using both experiment and theory.[25−27] Depending upon the Mo vapor concentration with respect to S, MoS_2 crystals can show different shapes (hexagon, truncated triangle, and triangle), sizes, and density variation as well as formation of MoO_2/$MoOS_2$ structures. Wang et al.[26] observed variations in the MoS_2 crystal shape from triangular to hexagonal geometries with respect to the distance from MoO_3 powdered precursor location. This variation in crystal shape was attributed to the variation of Mo vapor concentration along the growth substrate. Wu et al.[27] also observed shape and size variations of MoS_2 with respect to MoO_3 concentration. These studies suggest that there is a small window of Mo/S vapor ratio (both in Mo-rich and S-rich regions) during which the MoS_2 crystal can maintain triangular shape although their size could vary slightly because of a slight variation of Mo/S vapor ratio. With a relatively larger variation of vapor ratio, both shape and size

DOI: 10.1021/acsomega.8b02978
ACS Omega 2018, 3, 18943−18949

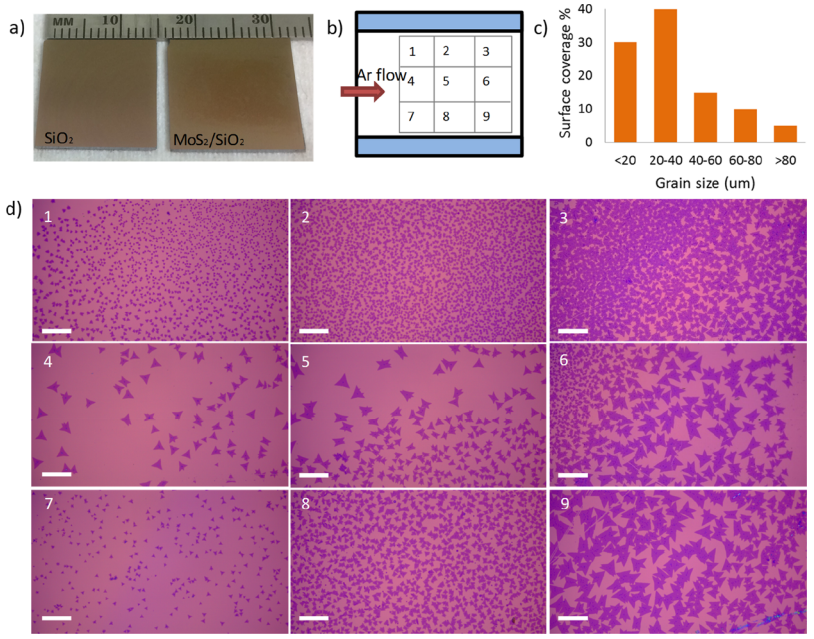

Figure 2. Growth results. (a) Contrast between bare Si/SiO_2 substrate and substrate after the growth of MoS_2. (b) Sketch of the sample with the corresponding image positions. The blue regions marked here are outside of the boat. (c) Grain-size histogram with the surface coverage. (d) Optical images of the substrate at the positions specified in (b). Scale bar is 100 μm in each image.

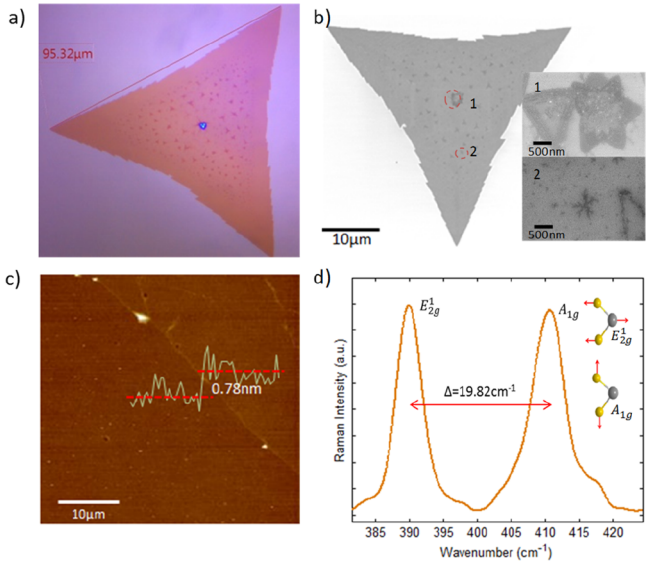

Figure 3. Characterization of the MoS_2 single crystals. (a) Optical image of one of the largest monolayer crystals observed. (b) SEM image of a single crystal. (c) AFM topography and height profile (inset) taken at an edge of a monolayer domain. (d) E^1_{2g} and A_{1g} vibrational modes of atoms and Raman single spectra for a single crystal.

can vary. Whereas too much of the Mo vapor variation could lead to MoS_2 in some places and $MoO_2/MoOS_2$ in other places. When MoO_3 powder was used as a precursor in our experiment (Figure S1), there appears to be a large variation of Mo/S vapor pressure throughout the growth region. On the other hand, when MoO_3 thin film was used as precursor for Mo vapor, we observe the same triangular crystal shape throughout the growth region (no shape variation, neither any oxysulfide species), suggesting that we are able to maintain a tight control on Mo vapor concentration in the gas phase by replacing the powdered precursor by the thin-film precursor.

Figure 2d also shows a size and density variation of the MoS_2 grains in different regions. A statistical view to the grain size variation is provided in Figure 2c. We observed crystal sizes up to 95 μm which is the largest we measured for this growth, and most crystals favored to grow in 20−40 μm size that covered around 40% of the growth region. The size variation and increased nucleation density are consistent with the picture of maintaining a tight control on the Mo vapor concentration discussed above. A slight spatial variation of the Mo/S vapor ratio because of a small variation of either Mo or S or both dictated by the flow, temperature gradients, and diffusion patterns within the gas can give rise to different sizes of MoS_2 crystals while maintaining triangular shape, even though Mo evaporation is homogenous. In some regions, triangular domains are merged to form polycrystalline aggregates[28] that can be seen because of the random orientations of the crystals and higher density.[28−31] Collectively, the absence of any oxysulfide phase along with the ability of maintaining triangular shape validates our capability to maintain a controlled Mo vapor condition for the clean growth of MoS_2.

In addition to MoS_2 grown on the growth substrate, we have occasionally observed scattered MoS_2 growth on source substrate as well (Figure S7), although the coverage density is much lower in comparison with the face-down growth substrate. This is an interesting observation, given the unique geometry of our growth setup, where Mo and S vapors are trapped between two parallel plates and the gas flow patterns also differ to the conventional face-down technique, where the growth substrate sits on top of a crucible with MoO_3 powder precursor. We note that a continuous coverage of monolayer MoS_2 was not obtained using our growth method neither on the growth substrate nor on the source substrate. The MoS_2 single crystal growth reported here using MoO_3 thin film as an evaporation source is different than the sulfurization of Mo

DOI: 10.1021/acsomega.8b02978
ACS Omega 2018, 3, 18943−18949

thin films previously reported by us and other groups.[32,33] In the present work, the reaction between Mo and S occurs in the vapor phase unlike the sulfurization of Mo thin films, where layer by layer sulfurization occurs at the thin film surface. In the present work, S was introduced to the reaction zone when the center of the furnace was at 650 °C. This is to ensure that all MoO_3 thin film was sublimated before S enters the reaction zone. In a control experiment (no S, all other parameters are identical to the optimized growth process), we found that 10 nm thin MoO_3 thin films were completely gone from the source substrate at a temperature of 550 °C (in atmospheric pressure). The resulting MoS_2 crystal qualities are also different as the grain size in the present work is tens of microns, whereas in the case of thin-film sulfurization, the grain size is tens of nanometers. As a result, the MoS_2 crystals grown using this method shows a very high crystal quality, uniformity, and better device properties discussed below, compared to the polycrystalline films obtained by thin-film sulfurization methods.

Figure 3a shows an optical micrograph of a single crystal grown with the size of ∼95 μm. These big crystals are mostly composed of monolayer regions along with some isolated dendritic bilayers[34−36] region which can be clearly seen in the SEM image as well (Figure 3b, spot 2). We only observe this bilayer formation in large size crystals which could be because of the added nucleation sites by the defects in the first layer.[36] The self-seeded nucleation center is also visible in the SEM image (Figure 3b, spot 1). The tapping-mode AFM image (Figure 3c) taken at a single-crystal edge was analyzed to identify the number of layers of the grown crystals. The step height at this edge was measured to be 0.78 nm which corresponds to the monolayer MoS_2 thickness, and the topography of the crystal shows a highly uniform layer. Raman single spectra (Figure 3d) was acquired to confirm the chemical composition of the material grown as well as the layer number. As shown in Figure 3c, Raman spectrum has two prominent peaks, E^1_{2g} and A_{1g}, which correspond to in-plane and out-of-plane vibrations of Mo and S atoms with respective wave numbers of 390.76 and 410.76 cm^{-1}, respectively. Spacing between these two peaks (Δ) is 19.82 cm^{-1} consistent with monolayer MoS_2.[37,38]

Figure 4a shows a PL spectrum from a representative single crystal with two signature peaks at 1.85 and 1.99 eV which corresponds to A (direct band gap excitations) and B (excitations resulted from valence band splitting because of strong spin−orbit coupling[39]) direct excitronic transitions.[37,40,41] The full width at half maximum of the A peak is measured to be ∼80 meV which is narrower than the exfoliated

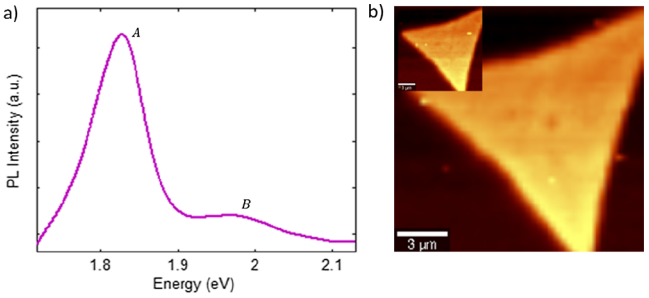

Figure 4. PL characterization. (a) PL single spectra of a MoS_2 crystal grown with the optimized growth recipe. (b) PL intensity mapping of A peak for the same crystal. Inset shows the mapping of B peak.

monolayer MoS_2 samples on Si/SiO_2 substrates[39,42] showing better optical quality of our samples. The even-color contrast of the PL intensity mapping of A and B peaks (Figure 4b) confirms the uniform layer thickness of the crystal.

Scanning TEM (STEM) was employed to further verify the crystal quality of the MoS_2 crystals. The as-grown MoS_2 crystals were transferred to a TEM grid with a carbon mesh using buffered oxide etchant (BOE; details in Materials and Methods). Figure 5 shows dark-field STEM (DF-STEM) micrographs for the monolayer MoS_2 grown using the thin-film-based coevaporation. High-resolution STEM (HRSTEM) image (Figure 5b) clearly shows the high crystalline quality of the monolayers with a periodic hexagonal atomic arrangement. The lattice constant is measured as 0.27 nm which agrees well with previously reported results.[29,43] The monolayer can also be identified from the folding edge of the transferred film (Figure 5c). Evidently in the SEM image, these big crystals show some multilayer growth at some regions (nucleation center and adlayers), and accordingly, the STEM data show Moire patterns caused by the diffraction because of the misalignment of these layers (Figure S5).

We also experimented this growth at higher temperatures. Figure S3 shows the optical micrographs of the crystals grown at 750, 800, and 850 °C by using 20 nm MoO_3 thin films. We observe triangular-shaped crystals at all growth temperature, suggesting that uniform Mo vapor pressure can be maintained at elevated temperature. We also found that the coverage density generally decreases at higher growth temperatures. This could be linked to the reduced nucleation at higher temperatures. The sticking coefficient which defines the nucleation ability of the surface significantly reduces because of the enhanced desorption rate at higher temperatures.[44] This phenomenon also explains the multilayer growth at the nucleation center at higher temperatures. There are less nucleation sites to facilitate the gas-phase MoS_2 to be adsorbed on to the substrate surface which results in the growth of multiple MoS_2 layers at the same nucleation site. The multilayer growth at high temperatures is discussed as an effect of a high precursor supply in the previous reports[31,45,46] when the MoO_3 powdered precursor is used which is not applicable for our thin-film-based growth. In our experiments even at 750 °C, MoO_3 thin film precursor is completely evaporated and reacted to grow MoS_2, therefore more MoO_3 supply is not possible. The AFM, Raman, and PL characterizations for the crystals grown at higher temperature are shown in Figure S4. The AFM topography shows a clear stepwise height variation, and each step height measured is similar to monolayer MoS_2 thickness. Raman single spectra taken near the center of nucleation show the E^1_{2g} and A_{1g} signature peaks for MoS_2 with the spacing of Δ = 23.43 cm^{-1} which corresponds to a few layers of MoS_2.[37,46] PL mapping of the crystals grown at 850 °C shows a clear PL intensity drop at these multilayers, and very thick layers at the center show no PL response. The effect of MoO_3 precursor amount is tested by varying the thickness of the film from 5 to 20 nm with the same amount of S (Figure S5). All of the crystals grown have a similar shape, suggesting that the uniform Mo pressure control is possible even with 5 nm thin film. However, the crystal sizes are reduced at lower thicknesses of MoO_3 because of the low-precursor supply.

We have also measured electrical transport properties of MoS_2 samples in a bottom-gated FET geometry. FET devices were fabricated on the as-grown MoS_2 single crystals by using

DOI: 10.1021/acsomega.8b02978
ACS Omega 2018, 3, 18943−18949

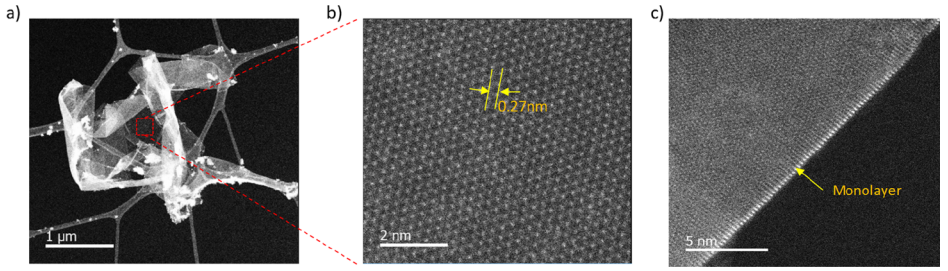

Figure 5. TEM characterization. (a) Low magnification DF-STEM image of the transferred thin film on the copper grid. (b) HRSTEM image of the monolayer MoS_2 showing hexagonal atom arrangement. (c) DF-STEM image for the folded edge of the monolayer.

standard electron beam lithography (EBL; see Materials and Methods). The nucleation center was excluded at the device fabrication to minimize the reflection of multiple layers in the transport measurements. We used nickel for source and drain electrodes. Linear I_D-V_D confirms that Ohmic contacts are formed at the two electrodes, and all of the measurements were performed under ambient conditions for the as-grown samples. Figure 6 shows electrical characteristics of a sample device

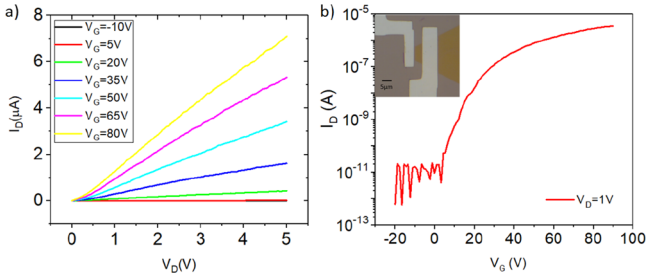

Figure 6. Electrical characteristics of the as-grown MoS_2 single crystals. (a) Output characteristics of the transistor device by sweeping the gate voltage (V_G) from −10 to 80 V. (b) Transfer characteristics. Plots are provided for the device shown in inset of (b).

(optical image is shown in the inset of Figure 6b). The field-effect mobility was extracted based on the slope dI_D/dV_G fitted to the linear region of the I_D-V_G using the equation $\mu = (L/WC_GV_D)(dI_D/dV_G)$, where L, W, and C_G are the channel length, channel width, and the gate capacitance. For the sample device shown in the figure, 5 μm channel length and 6 μm channel width are used in mobility calculations. This device shows an n-type conduction with an on/off ratio of 10^6 and peak mobility ~4.5 cm^2/V s, which is comparable with the mobilities for pristine devices fabricated on CVD-grown monolayers in previous reports.[28]

CONCLUSIONS

In conclusion, we introduced a new CVD-based method to synthesize monolayer MoS_2 crystals by using MoO_3 thin films as a precursor for coevaporation. This new method facilitates uniform vapor pressure of Mo, resulting in a clean single-crystal growth of MoS_2 throughout the substrate, and is highly reproducible. The as-grown MoS_2 crystals show excellent Raman and PL response corresponding to high-quality single crystals. TEM characterization further confirms the crystalline quality of the sample. Room-temperature electrical transport measurements show a mobility of ~5 cm^2/V s with a current on/off ratio of 10^6. We believe this new CVD process can be used for the synthesis of other TMDC materials, and the growth can be extended to a wide range of substrate types.

MATERIALS AND METHODS

Growth Process. Si substrates with 250 nm thick oxide layer were used as growth substrates as well as the substrates to deposit the MoO_3 thin films which were used as a precursor for coevaporation. The substrate was cleaned via sonication in acetone for 5 min, followed by sonication in isopropyl alcohol (IPA) for 5 min, deionized water rinse, and 10 min mild oxygen plasma treatment. MoO_3 thin films with the thickness of 5−20 nm were deposited using thermal evaporation of MoO_3 powder (99.5%, Sigma-Aldrich) in a vacuum chamber at low evaporation rates of 0.2−0.5 A/s. The thickness of these thin films was confirmed via AFM topography (Figure S6). The thin-film-deposited substrates were cut into 1 cm × 1 cm size and placed in a ceramic boat; bare target substrates were placed on the same boat facing down with the separation (Figure 1b) of 3−4 mm toward the source and placed at the center of the furnace. Although the front end of the boat was left open for sulfur vapors to enter the reaction zone easily, the rear end was covered by the substrate to trap the vapor phase precursors near the substrate, but a small spacing (less than a mm) was left at the end to ensure that the sulfur vapor pressure does not overstep the balance between precursors. Ceramic crucible containing 600 mg of S powder (99.5%, Sigma-Aldrich) was loaded in to a 1 in. quartz tube placed at the edge of the tube furnace (Barnstead International F79300 Tube Furnace) upstream. For different temperature setpoints, the MoO_3 and S precursor distance (r) is adjusted accordingly in such a way that S starts melting below 100° from the setpoint value. Argon gas (99.995% purity) was used as the carrier gas. Temperature of the furnace was raised to the growth temperature of 750−850 °C at the rate of 20 °C/min and held for 10 min (dwell time). After the dwell time, the furnace could cool down naturally until the temperature dropped to 500 °C at which point, the furnace hood was opened for rapid cooling. The Ar flow (200 sccm) was passed initially before heating up the furnace for 10 min to saturate the environment with argon, after which the flow rate was kept constant at 10 sccm. For the parameters used in this process, we found that 10 sccm gas flow with 10 min dwell time is optimum for our growth. When the temperature of the furnace dropped to 350 °C, it was purged with 200 sccm Ar again to flush off the excess reactants.

Characterization of the Materials. The surface imaging and the grain size measurements were carried out by an Olympus BX51M microscope equipped with a Jenoptic Progres Gryphax camera, and the SEM images were taken with a Zeiss ULTRA-55 FEG SEM. A tapping-mode AFM (Veeco instruments, Dimension 3100) topography was used to determine the height of MoS_2 crystals. The samples were scanned at slow rates in small scan areas at the edge of MoS_2

DOI: 10.1021/acsomega.8b02978
ACS Omega 2018, 3, 18943−18949

crystal to achieve more accurate height profiles. Raman and PL spectroscopy measurements were carried out with confocal Raman microscope (WITec Alpha 300 RA) at an excitation wavelength of 532 nm and with laser power of 0.293 mW at ambient conditions. For TEM characterizations, a droplet of BOE was placed on the Si/SiO_2 substrate where MoS_2 crystals were grown. After a few minutes, the oxide layer was etched and the crystals were transferred to the liquid. The liquid was then picked up by a clean syringe and released on a TEM grid with a carbon mesh. All TEM/STEM measurements were performed with a JEOL ARM200F FEG-TEM/STEM with a Cs-corrector.

Device Fabrication and Transport Measurements. The bottom-gated FETs for the transport measurements were fabricated using standard EBL using a Nabity Pattern Generator System connected to a Zeiss ultra 55 SEM for selected single crystals. Poly(methyl methacrylate) was spin-coated on to the substrate containing MoS_2 samples and baked at 130 °C for 3 min. The source and drain electrodes were then defined using EBL and developed in a solution of methyl isobutyl ketone and IPA. A 30 nm thick Ni film was deposited for the metal contacts using E-beam evaporation. The electron transport measurements of the final MoS_2 devices were carried out in a room temperature probe station using a Keysight Semiconductor Device Analyzer.

■ ASSOCIATED CONTENT

Supporting Information

The Supporting Information is available free of charge on the ACS Publications website at DOI: 10.1021/acsomega.8b02978.

> Additional information on growth results for coevaporation of MoO_3 and sulfur powders, lateral substrate placement growth, growth at different temperatures, characterization of multilayer growth at higher temperature, effect of MoO_3 film thickness, supplementary TEM images, MoS_2 growth on source substrate, and AFM characterization of thin film MoO_3 source (PDF)

■ AUTHOR INFORMATION

Corresponding Author

*E-mail: saiful@ucf.edu (S.I.K.).

ORCID

Tania Roy: 0000-0003-1131-8068

Yeonwoong Jung: 0000-0001-6042-5551

Saiful I. Khondaker: 0000-0003-1333-1928

Notes

The authors declare no competing financial interest.

■ ACKNOWLEDGMENTS

This work was supported by the U.S. National Science Foundation (NSF) under grant no. 1728309. We also acknowledge Dr. Tetard for Raman/PL spectroscopy support.

■ REFERENCES

(1) Cunningham, G.; Khan, U.; Backes, C.; Hanlon, D.; McCloskey, D.; Donegan, J. F.; Coleman, J. N. Photoconductivity of solution-processed MoS2 films. *J. Mater. Chem. C* **2013**, *1*, 6899−6904.

(2) Perea-López, N.; Elías, A. L.; Berkdemir, A.; Castro-Beltran, A.; Gutiérrez, H. R.; Feng, S.; Lv, R.; Hayashi, T.; López-Urías, F.; Ghosh, S.; Muchharla, B.; Talapatra, S.; Terrones, H.; Terrones, M. Photosensor Device Based on Few-Layered WS2 Films. *Adv. Funct. Mater.* **2013**, *23*, 5511−5517.

(3) Radisavljevic, B.; Radenovic, A.; Brivio, J.; Giacometti, V.; Kis, A. Single-layer MoS2 transistors. *Nat. Nanotechnol.* **2011**, *6*, 147−150.

(4) Lopez-Sanchez, O.; Lembke, D.; Kayci, M.; Radenovic, A.; Kis, A. Ultrasensitive photodetectors based on monolayer MoS2. *Nat. Nanotechnol.* **2013**, *8*, 497−501.

(5) Salehzadeh, O.; Tran, N. H.; Liu, X.; Shih, I.; Mi, Z. Exciton Kinetics, Quantum Efficiency, and Efficiency Droop of Monolayer MoS2 Light-Emitting Devices. *Nano Lett.* **2014**, *14*, 4125−4130.

(6) Tsai, M.-L.; Su, S.-H.; Chang, J.-K.; Tsai, D.-S.; Chen, C.-H.; Wu, C.-I.; Li, L.-J.; Chen, L.-J.; He, J.-H. Monolayer MoS2 Heterojunction Solar Cells. *ACS Nano* **2014**, *8*, 8317−8322.

(7) Sarkar, D.; Liu, W.; Xie, X.; Anselmo, A. C.; Mitragotri, S.; Banerjee, K. MoS2 Field-Effect Transistor for Next-Generation Label-Free Biosensors. *ACS Nano* **2014**, *8*, 3992−4003.

(8) Wang, L.; Wang, Y.; Wong, J. I.; Palacios, T.; Kong, J.; Yang, H. Y. Functionalized MoS2 Nanosheet-Based Field-Effect Biosensor for Label-Free Sensitive Detection of Cancer Marker Proteins in Solution. *Small* **2014**, *10*, 1101−1105.

(9) Naylor, C. H.; Kybert, N. J.; Schneier, C.; Xi, J.; Romero, G.; Saven, J. G.; Liu, R.; Johnson, A. T. C. Scalable Production of Molybdenum Disulfide Based Biosensors. *ACS Nano* **2016**, *10*, 6173−6179.

(10) Zhan, Y.; Liu, Z.; Najmaei, S.; Ajayan, P. M.; Lou, J. Large-Area Vapor-Phase Growth and Characterization of MoS2 Atomic Layers on a SiO2 Substrate. *Small* **2012**, *8*, 966−971.

(11) Kong, D.; Wang, H.; Cha, J. J.; Pasta, M.; Koski, K. J.; Yao, J.; Cui, Y. Synthesis of MoS2 and MoSe2 Films with Vertically Aligned Layers. *Nano Lett.* **2013**, *13*, 1341−1347.

(12) Lin, Y.-C.; Zhang, W.; Huang, J.-K.; Liu, K.-K.; Lee, Y.-H.; Liang, C.-T.; Chu, C.-W.; Li, L.-J. Wafer-scale MoS2 thin layers prepared by MoO3 sulfurization. *Nanoscale* **2012**, *4*, 6637−6641.

(13) Liu, K.-K.; Zhang, W.; Lee, Y.-H.; Lin, Y.-C.; Chang, M.-T.; Su, C.-Y.; Chang, C.-S.; Li, H.; Shi, Y.; Zhang, H.; Lai, C.-S.; Li, L.-J. Growth of Large-Area and Highly Crystalline MoS2 Thin Layers on Insulating Substrates. *Nano Lett.* **2012**, *12*, 1538−1544.

(14) Huang, C.-C.; Al-Saab, F.; Wang, Y.; Ou, J.-Y.; Walker, J. C.; Wang, S.; Gholipour, B.; Simpson, R. E.; Hewak, D. W. Scalable high-mobility MoS2 thin films fabricated by an atmospheric pressure chemical vapor deposition process at ambient temperature. *Nanoscale* **2014**, *6*, 12792−12797.

(15) Dumcenco, D.; Ovchinnikov, D.; Marinov, K.; Lazić, P.; Gibertini, M.; Marzari, N.; Sanchez, O. L.; Kung, Y.-C.; Krasnozhon, D.; Chen, M.-W.; Bertolazzi, S.; Gillet, P.; Fontcuberta i Morral, A. F. i.; Radenovic, A.; Kis, A. Large-Area Epitaxial Monolayer MoS2. *ACS Nano* **2015**, *9*, 4611−4620.

(16) Smithe, K. K. H.; English, C. D.; Suryavanshi, S. V.; Pop, E. Intrinsic electrical transport and performance projections of synthetic monolayer MoS2 devices. *2D Mater.* **2016**, *4*, 011009.

(17) Chen, J.; Tang, W.; Tian, B.; Liu, B.; Zhao, X.; Liu, Y.; Ren, T.; Liu, W.; Geng, D.; Jeong, H. Y.; Shin, H. S.; Zhou, W.; Loh, K. P. Chemical Vapor Deposition of High-Quality Large-Sized MoS2 Crystals on Silicon Dioxide Substrates. *Adv. Sci.* **2016**, *3*, 1500033.

(18) Li, M.; Chen, J.-S.; Routh, P. K.; Zahl, P.; Nam, C.-Y.; Cotlet, M. Distinct Optoelectronic Signatures for Charge Transfer and Energy Transfer in Quantum Dot−MoS2 Hybrid Photodetectors Revealed by Photocurrent Imaging Microscopy. *Adv. Funct. Mater.* **2018**, *28*, 1707558.

(19) Pondick, J. V.; Woods, J. M.; Xing, J.; Zhou, Y.; Cha, J. J. Stepwise Sulfurization from MoO3 to MoS2 via Chemical Vapor Deposition. *ACS Appl. Nano Mater.* **2018**, *1*, 5655−5661.

(20) Lee, J.; Pak, S.; Giraud, P.; Lee, Y.-W.; Cho, Y.; Hong, J.; Jang, A.-R.; Chung, H.-S.; Hong, W.-K.; Jeong, H. Y.; Shin, H. S.; Occhipinti, L. G.; Morris, S. M.; Cha, S.; Sohn, J. I.; Kim, J. M. Thermodynamically Stable Synthesis of Large-Scale and Highly Crystalline Transition Metal Dichalcogenide Monolayers and their Unipolar n−n Heterojunction Devices. *Adv. Mater.* **2017**, *29*, 1702206.

DOI: 10.1021/acsomega.8b02978
ACS Omega 2018, 3, 18943−18949

(21) Li, X. L.; Li, Y. D. Formation MoS2 inorganic fullerenes (IFs) by the reaction of MoO3 nanobelts and S. *Chem.—Eur. J.* **2003**, *9*, 2726−2731.
(22) Cain, J. D.; Shi, F.; Wu, J.; Dravid, V. P. Growth Mechanism of Transition Metal Dichalcogenide Monolayers: The Role of Self-Seeding Fullerene Nuclei. *ACS Nano* **2016**, *10*, 5440−5445.
(23) Najmaei, S.; Liu, Z.; Zhou, W.; Zou, X.; Shi, G.; Lei, S.; Yakobson, B. I.; Idrobo, J.-C.; Ajayan, P. M.; Lou, J. Vapour phase growth and grain boundary structure of molybdenum disulphide atomic layers. *Nat. Mater.* **2013**, *12*, 754−759.
(24) Liu, H.; Zhu, Y.; Meng, Q.; Lu, X.; Kong, S.; Huang, Z.; Jiang, P.; Bao, X. Role of the carrier gas flow rate in monolayer MoS2 growth by modified chemical vapor deposition. *Nano Res.* **2016**, *10*, 643−651.
(25) Rajan, A. G.; Warner, J. H.; Blankschtein, D.; Strano, M. S. Generalized Mechanistic Model for the Chemical Vapor Deposition of 2D Transition Metal Dichalcogenide Monolayers. *ACS Nano* **2016**, *10*, 4330−4344.
(26) Wang, S.; Rong, Y.; Fan, Y.; Pacios, M.; Bhaskaran, H.; He, K.; Warner, J. H. Shape Evolution of Monolayer MoS2 Crystals Grown by Chemical Vapor Deposition. *Chem. Mater.* **2014**, *26*, 6371−6379.
(27) Wu, S.; Zeng, X.; Wang, W.; Zeng, Y.; Hu, Y.; Yin, S.; Lu, J.; Zhou, G. The morphological control of MoS2 films using a simple model under chemical vapor deposition. *Thin Solid Films* **2018**, *666*, 150−155.
(28) van der Zande, A. M.; Huang, P. Y.; Chenet, D. A.; Berkelbach, T. C.; You, Y.; Lee, G.-H.; Heinz, T. F.; Reichman, D. R.; Muller, D. A.; Hone, J. C. Grains and grain boundaries in highly crystalline monolayer molybdenum disulphide. *Nat. Mater.* **2013**, *12*, 554−561.
(29) Ji, Q.; Kan, M.; Zhang, Y.; Guo, Y.; Ma, D.; Shi, J.; Sun, Q.; Chen, Q.; Zhang, Y.; Liu, Z. Unravelling Orientation Distribution and Merging Behavior of Monolayer MoS2 Domains on Sapphire. *Nano Lett.* **2014**, *15*, 198−205.
(30) Chen, J.; Tang, W.; Tian, B.; Liu, B.; Zhao, X.; Liu, Y.; Ren, T.; Liu, W.; Geng, D.; Jeong, H. Y.; Shin, H. S.; Zhou, W.; Loh, K. P. Chemical Vapor Deposition of High-Quality Large-Sized MoS2 Crystals on Silicon Dioxide Substrates. *Adv. Sci.* **2016**, *3*, 1500033.
(31) Gong, Y.; Ye, G.; Lei, S.; Shi, G.; He, Y.; Lin, J.; Zhang, X.; Vajtai, R.; Pantelides, S. T.; Zhou, W.; Li, B.; Ajayan, P. M. Synthesis of Millimeter-Scale Transition Metal Dichalcogenides Single Crystals. *Adv. Funct. Mater.* **2016**, *26*, 2009−2015.
(32) Islam, M. A.; Kim, J. H.; Schropp, A.; Kalita, H.; Choudhary, N.; Weitzman, D.; Khondaker, S. I.; Oh, K. H.; Roy, T.; Chung, H.-S.; Jung, Y. Centimeter-Scale 2D van der Waals Vertical Heterostructures Integrated on Deformable Substrates Enabled by Gold Sacrificial Layer-Assisted Growth. *Nano Lett.* **2017**, *17*, 6157−6165.
(33) Choudhary, N.; Park, J.; Hwang, J. Y.; Chung, H.-S.; Dumas, K. H.; Khondaker, S. I.; Choi, W.; Jung, Y. Centimeter Scale Patterned Growth of Vertically Stacked Few Layer Only 2D MoS2/WS2 van der Waals Heterostructure. *Sci. Rep.* **2016**, *6*, 25456.
(34) Liu, Y.; Ghosh, R.; Wu, D.; Ismach, A.; Ruoff, R.; Lai, K. Mesoscale Imperfections in MoS2 Atomic Layers Grown by a Vapor Transport Technique. *Nano Lett.* **2014**, *14*, 4682−4686.
(35) Yore, A. E.; Smithe, K. K. H.; Crumrine, W.; Miller, A.; Tuck, J. A.; Redd, B.; Pop, E.; Wang, B.; Newaz, A. K. M. Visualization of Defect-Induced Excitonic Properties of the Edges and Grain Boundaries in Synthesized Monolayer Molybdenum Disulfide. *J. Phys. Chem. C* **2016**, *120*, 24080−24087.
(36) Wang, X.; Gong, Y.; Shi, G.; Chow, W. L.; Keyshar, K.; Ye, G.; Vajtai, R.; Lou, J.; Liu, Z.; Ringe, E.; Tay, B. K.; Ajayan, P. M. Chemical Vapor Deposition Growth of Crystalline Monolayer MoSe2. *ACS Nano* **2014**, *8*, 5125−5131.
(37) Lee, C.; Yan, H.; Brus, L. E.; Heinz, T. F.; Hone, J.; Ryu, S. Anomalous lattice vibrations of single- and few-layer MoS2. *ACS Nano* **2010**, *4*, 2695−2700.
(38) Sanne, A.; Ghosh, R.; Rai, A.; Yogeesh, M. N.; Shin, S. H.; Sharma, A.; Jarvis, K.; Mathew, L.; Rao, R.; Akinwande, D.; Banerjee, S. Radio Frequency Transistors and Circuits Based on CVD MoS2. *Nano Lett.* **2015**, *15*, 5039−5045.
(39) Zhang, J.; Yu, H.; Chen, W.; Tian, X.; Liu, D.; Cheng, M.; Xie, G.; Yang, W.; Yang, R.; Bai, X.; Shi, D.; Zhang, G. Scalable Growth of High-Quality Polycrystalline MoS2 Monolayers on SiO2 with Tunable Grain Sizes. *ACS Nano* **2014**, *8*, 6024−6030.
(40) Mak, K. F.; Lee, C.; Hone, J.; Shan, J.; Heinz, T. F. Atomically Thin MoS2: A New Direct-Gap Semiconductor. *Phys. Rev. Lett.* **2010**, *105*, 136805.
(41) Choudhary, N.; Islam, M. R.; Kang, N.; Tetard, L.; Jung, Y.; Khondaker, S. I. Two-dimensional lateral heterojunction through bandgap engineering of MoS2 via oxygen plasma. *J. Phys.: Condens. Matter* **2016**, *28*, 364002.
(42) Kang, N.; Paudel, H. P.; Leuenberger, M. N.; Tetard, L.; Khondaker, S. I. Photoluminescence Quenching in Single-Layer MoS2 via Oxygen Plasma Treatment. *J. Phys. Chem. C* **2014**, *118*, 21258−21263.
(43) Liang, T.; Xie, S.; Huang, Z.; Fu, W.; Cai, Y.; Yang, X.; Chen, H.; Ma, X.; Iwai, H.; Fujita, D.; Hanagata, N.; Xu, M. Elucidation of Zero-Dimensional to Two-Dimensional Growth Transition in MoS2 Chemical Vapor Deposition Synthesis. *Adv. Mater. Interfaces* **2016**, *4*, 1600687.
(44) Yue, R.; Nie, Y.; Walsh, L. A.; Addou, R.; Liang, C.; Lu, N.; Barton, A. T.; Zhu, H.; Che, Z.; Barrera, D.; Cheng, L.; Cha, P.-R.; Chabal, Y. J.; Hsu, J. W. P.; Kim, J.; Kim, M. J.; Colombo, L.; Wallace, R. M.; Cho, K.; Hinkle, C. L. Nucleation and growth of WSe2: enabling large grain transition metal dichalcogenides. *2D Mater.* **2017**, *4*, 045019.
(45) Zhou, H.; Wang, C.; Shaw, J. C.; Cheng, R.; Chen, Y.; Huang, X.; Liu, Y.; Weiss, N. O.; Lin, Z.; Huang, Y.; Duan, X. Large area growth and electrical properties of p-type WSe2 atomic layers. *Nano Lett.* **2014**, *15*, 709−713.
(46) Zhou, D.; Shu, H.; Hu, C.; Jiang, L.; Liang, P.; Chen, X. Unveiling the Growth Mechanism of MoS2 with Chemical Vapor Deposition: From Two-Dimensional Planar Nucleation to Self-Seeding Nucleation. *Cryst. Growth Des.* **2018**, *18*, 1012−1019.

DOI: 10.1021/acsomega.8b02978
ACS Omega 2018, 3, 18943−18949